

## Vertical velocity and transport in the South China Sea

Yaohua Zhu<sup>1,2,3</sup>, Dingqi Wang<sup>1,4</sup>, Yonggang Wang<sup>1,2,3</sup>, Shujiang Li<sup>1,2,3</sup>, Tengfei Xu<sup>1,2,3</sup>, Zexun Wei<sup>1,2,3\*</sup>

<sup>1</sup>First Institute of Oceanography, and Key Laboratory of Marine Science and Numerical Modeling, Ministry of Natural Resources, Qingdao 266061, China

<sup>2</sup>Laboratory for Regional Oceanography and Numerical Modeling, Pilot National Laboratory for Marine Science and Technology (Qingdao), Qingdao 266237, China

<sup>3</sup>Shandong Key Laboratory of Marine Science and Numerical Modeling, Qingdao 266061, China

<sup>4</sup>College of Oceanic and Atmospheric Sciences, Ocean University of China, Qingdao 266100, China

Received 4 August 2021; accepted 12 October 2021

© Chinese Society for Oceanography and Springer-Verlag GmbH Germany, part of Springer Nature 2022

### Abstract

Deep water in the South China Sea is renewed by the cold and dense Luzon Strait overflow. However, from where and how the deep water upwells is poorly understood yet. Based on the Hybrid Coordinate Ocean Model reanalysis data, vertical velocity is derived to answer these questions. Domain-integrated vertical velocity is of two maxima, one in the shallow water and the other at depth, and separated by a layer of minimum at the bottom of the thermocline. Further analysis shows that this two-segmented vertical transport is attributed to the vertical compensation of subsurface water to the excessive outflow of shallow water and upward push of the dense Luzon Strait overflow, respectively. In the abyssal basin, the vertical transport increases upward from zero at the depth of 3 500–4 000 m and reaches a maximum of  $1.5 \times 10^6$  m<sup>3</sup>/s at about 1 500 m. Deep water upwells mainly from the northeastern and southwestern ends of the abyssal basin and off the continental slopes. To explain the upward velocity arising from slope breaks, a possible mechanism is proposed that an onshore velocity component can be derived from the deep western boundary current above steep slopes under bottom friction.

**Key words:** vertical velocity, vertical transport, Luzon Strait overflow, South China Sea

**Citation:** Zhu Yaohua, Wang Dingqi, Wang Yonggang, Li Shujiang, Xu Tengfei, Wei Zexun. 2022. Vertical velocity and transport in the South China Sea. *Acta Oceanologica Sinica*, 41(7): 13–25, doi: 10.1007/s13131-021-1954-4

### 1 Introduction

The South China Sea (SCS) covers an area of  $3.5 \times 10^6$  km<sup>2</sup>, including  $1.68 \times 10^6$  km<sup>2</sup> on continental shelves,  $1.26 \times 10^6$  km<sup>2</sup> on slopes and  $0.55 \times 10^6$  km<sup>2</sup> in the abyssal basin below 3 000 m (Fig. 1). In view of the 200 m isobath, it is a semienclosed oceanic basin (Wang, 1986). The SCS connects to the western Pacific through its sole deepwater renewal channel, the Luzon Strait, with the deepest sill at about 2 400 m. Below the depth of 1 500 m, the density on both sides of the Luzon Strait bifurcates, and water is denser on the Pacific side than that on the SCS side. As a result, there exists a persistent pressure gradient across the Luzon Strait, driving a so-called Luzon Strait deepwater overflow from the Pacific into the SCS (Nitani, 1972; Qu et al., 2006; Li and Qu, 2006; Zhao et al., 2014; Zhang et al., 2015). The bifurcation depth of water density, about 1 500 m, is thus considered as the upper interface of the Luzon Strait overflow. After the dense Pacific water sinks into the SCS through the gaps in the Heng-Chun Ridge, the abyssal water in the SCS is renewed and must upwell somewhere. Then, scientific questions arise. At what depth and from where the abyssal water upwells? What is the causal mechanism?

Vertical velocity in the SCS has been studied as an important index of regional upwelling and downwelling. Among previous studies, Chai et al. (2001) analyzed formation of upwelling in the nearshore areas and Gan et al. (2013) focused on dynamics of the intensified downwelling over a widened northern SCS continent-

al shelf. Xie et al. (2012), Jing et al. (2015) and Xie et al. (2017) investigated the vertical circulation and its dynamics on the continental shelf east of Hainan Island. Qu (2000) and Qu et al. (2007) discussed offshore upwelling in the upper layer using historical temperature profiles, while Chao et al. (1996), Shu et al. (2014), and Cai and Gan (2020) analyzed vertical velocity in the deep layer using numerical models. Until now, an overall look of the vertical velocity and associated transport in the SCS basin scale is not in focus yet, however, it is an important part of vertical circulation and also links the layered horizontal circulation. Our objective of this study is to reveal the spatial pattern of vertical velocity and structure of vertical transport. Further, we devote to the mechanism how the vertical velocity arises from the abyssal basin, and mechanism how the vertical transport is forced. Finally, we analyze the role of vertical velocity and vertical transport, and then diagram the three-dimensional circulation in the SCS.

The rest of the paper is organized as follows. In Section 2, we describe the method and validate the data used in this study. Section 3 is devoted to the vertical velocity and mechanism of the vertical transport in the thermocline. Section 4 focuses on the vertical velocity and transport in the deepwater cell. A possible mechanism of upward velocity in the abyssal basin is proposed in Section 5, followed by a summary and conclusions in Section 6.

Foundation item: The National Key Research and Development Program of China under contract No. 2019YFC1408400; the National Natural Science Foundation of China under contract Nos 41876029, 41821004 and 41776042.

\*Corresponding author, E-mail: [weizx@fio.org.cn](mailto:weizx@fio.org.cn)

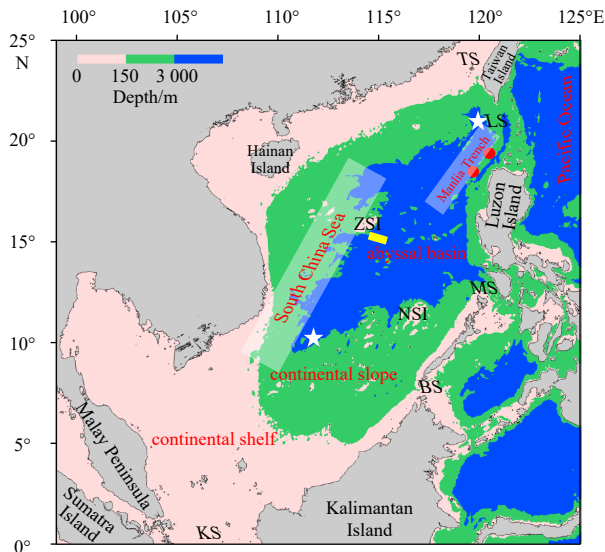


**Fig. 1.** Topography of the South China Sea. The abbreviations LS, TS, KS, MS, BS denote the Luzon Strait, Taiwan Strait, Karimata Strait, Mindoro Strait, Balabac Strait, respectively; and ZSI and NSI denote the Zhongsha Islands and Nansha Islands, respectively. Yellow line indicates the mooring section deployed off the Zhongsha Islands in Zhou et al. (2017). White stars represent the northern and southern ends of the abyssal basin below 3 000 m, where the abyssal water upwells. Red dots stand for gaps in the Heng-Chun Ridge, through which the Luzon Strait overflow sinks into the Manila Trench.

## 2 Data and methods

### 2.1 Data

The 22-year (1994–2015) product of Hybrid Coordinate Ocean Model+Navy Coupled Ocean Data Assimilation (HYCOM+NCODA) (1/12°) reanalysis run by the Naval Research Laboratory of U.S. Navy is analyzed in this study (available at <http://hycom.org/dataserver/glb-reanalysis>). This HYCOM Global Ocean Forecasting System (GOF3.1) reanalysis is of significant improvements over its previous version, GOF3.0. In detail, it has 17 terms in the equation of state, instead of only 7 terms in the GOF3.0 version; it has 41 vertical layers, instead of only 32 layers in the GOF3.0; it calculates wind stress using sea surface temperature (SST) and taking into account surface currents, instead of reading in the off-line wind stress in the previous version. The HYCOM GOF3.1 also has advantages in calculating ocean turbidity from monthly chlorophyll climatology, instead of using photosynthetically available radiation in the GOF3.0; it uses weaker sea surface salinity (SSS) relaxation, instead of strong relaxation in the GOF3.0 version.

### 2.2 Validation of HYCOM GOF3.1 reanalysis

As vertical velocity in the thermocline and deep cells will be discussed in the following sections, here we validate the HYCOM GOF3.1 reanalysis with observations in both shallow water and deep layer, respectively. The most remarkable feature in the deep SCS circulation is the deep western boundary current (DWBC). Among all the available *in situ* current observations in the DWBC, the velocity profiles east of Zhongsha Islands with 6 moorings during August 2012 to January 2014 observed by Zhou et al. (2017) are probably the longest mooring data. The time-mean alongshore velocity from observations manifests a southwest-

ward DWBC core leaning on the continental slope margin with a maximum magnitude of 2 cm/s and standard deviation (STD) up to 5 cm/s above the bottom (Fig. 2a). These main features are favorably simulated by the HYCOM GOF3.1 reanalysis albeit the DWBC core is overestimated. The standard deviation in the DWBC core from the HYCOM reaches 4.5 cm/s, corresponding well to the observations (Fig. 2b). The discrepancies of core depth, strength and thickness of the DWBC between the HYCOM GOF3.1 reanalysis and the mooring observations are probably due to the coarse vertical resolution in the model (with a layer thickness of 500 m near the bottom) and topographic difference between reality and numerical model. The monthly mean alongshore velocity in the DWBC core reaches its maximum in April, 7.2 cm/s from the observations (Fig. 2c) and 6.8 cm/s from the HYCOM reanalysis (Fig. 2d). The monthly climatology of the DWBC from both observations and HYCOM reanalysis shows a robust southwestward core from April to September and weak DWBC from October to March. Considering the velocity in the deep layer is much more difficult to simulate than that near the sea surface and the flow is not constrained by the data assimilation below 2 000 m, the HYCOM GOF3.1 reanalysis is deemed to reproduce the bottom-intensified DWBC and show a decent agreement with the long-term observations in the location, strength, standard deviation, and monthly climatology of the DWBC core.

Time-series of volume transport is often used to examine model results. Among all the main passages connecting the SCS and adjacent oceans, the Karimata Strait is of the longest record of volume transport estimated with direct measurements of current and satellite observations from 2008 to 2016 (Xu et al., 2021). For a better comparison, this observational transport series is extended based on sea surface height and local wind from satellite to cover the HYCOM GOF3.1 reanalysis. The 22-year monthly mean volume transport through the Karimata Strait from the HYCOM is depicted in Fig. 3a (black line). It agrees well with observational monthly mean transport (red line). The time-mean transport is  $0.82 \times 10^6 \text{ m}^3/\text{s}$  southward from observations and  $0.62 \times 10^6 \text{ m}^3/\text{s}$  southward from the HYCOM GOF3.1 reanalysis, which is well within the standard error of estimate from the observations ( $0.48 \times 10^6 \text{ m}^3/\text{s}$ ). In the meantime, the HYCOM GOF3.1 reanalysis captures the temporal variability of the transport fairly well. The correlation coefficient between the two transport time series is 0.98 and above the 95% confidence level.

The temporal variability of the Luzon Strait overflow is also examined. The longest record of the Luzon Strait overflow is the 3.5-year continuously mooring-observed along channel velocity (Zhou et al., 2014). The HYCOM GOF3.1 reanalysis captures an in phase annual cycle with the mooring observations (Fig. 3b). The correlation coefficient between them is 0.60 and above the 95% confidence level. As there is no data assimilation in the abyssal channel, the deepwater flow is always much harder to simulate than the shallow flow does. In addition, deepwater flow is highly topography steered and topography discrepancy does exist between the reality and model. In this sense, we deem the HYCOM GOF3.1 reanalysis is consistent with observations in both shallow water and deep layer, and thus believe the decent validation of the HYCOM reanalysis may provide a good opportunity in its performance in simulating vertical velocity and transport in the SCS.

### 2.3 Methods

Over step-like bottom topography as is in the numerical model, vertical velocity is zero at the locally flat ocean floor. Hence,

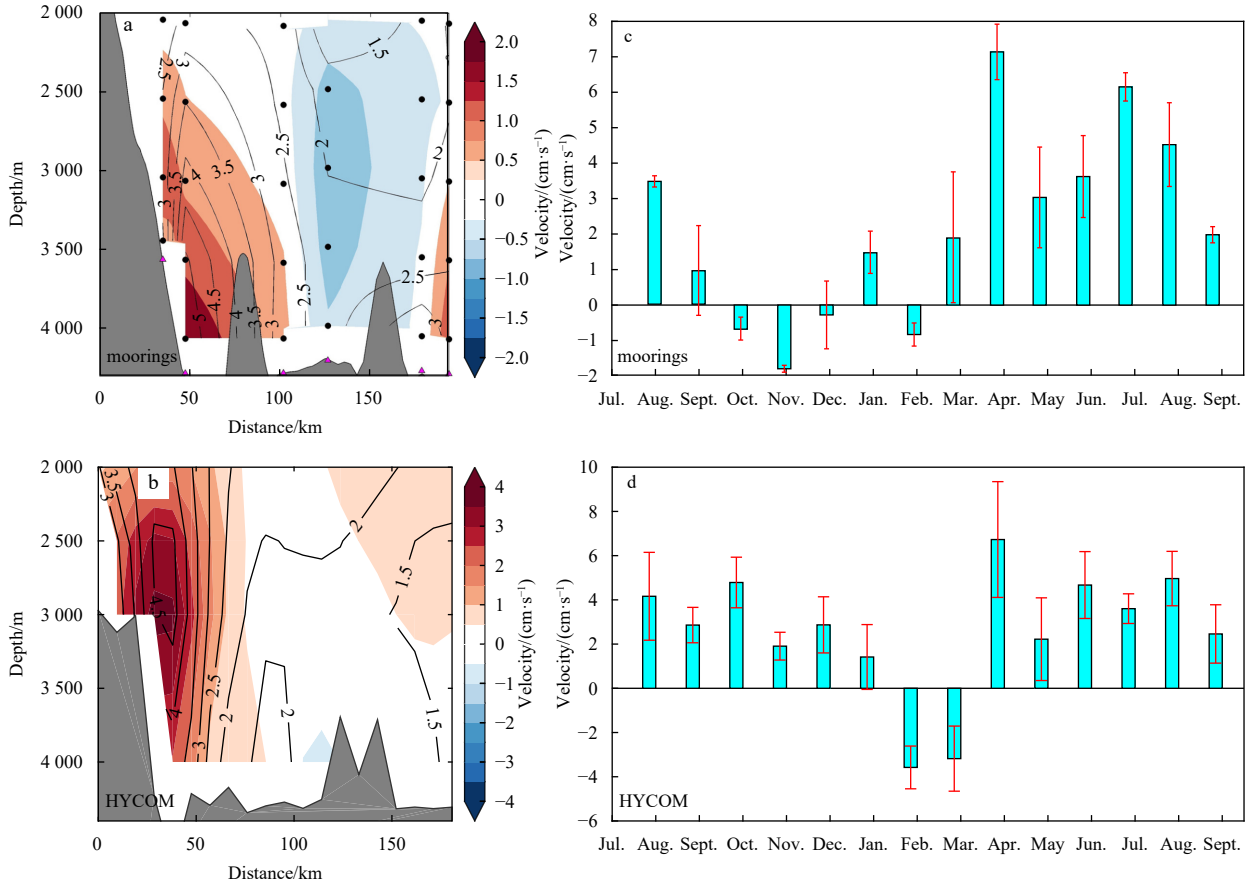


**Fig. 2.** Time-mean alongshore velocity in the deep western boundary current (DWBC) east of Zhongsha Islands from mooring observations (a), after Zhou et al. (2017), and HYCOM GOFS3.1 reanalysis (b). In a and b, color shading indicates the time-mean velocity, positive southwestward. Gray shading represents the topography. Black lines stand for the standard deviation of the alongshore velocity. Monthly mean alongshore velocity in the DWBC core east of Zhongsha Islands during August 2012 to September 2013 from mooring observations (c), after Zhou et al. (2017), and HYCOM GOFS3.1 reanalysis (d). In c and d, standard deviations are indicated by red bars.

the vertical velocity is calculated by depth-integrating the divergence of horizontal velocity,

$$w_{(z)} = -\nabla_{\mathbf{h}} \cdot \int_{-H}^z \vec{V}_{\mathbf{h}} dz, \quad (1)$$

where  $H$  is the bottom depth,  $\vec{V}_{\mathbf{h}}$  is the horizontal velocity vector and  $z$  is the depth. To remove grid-scale noise, horizontal smoothing operations are normally used. For example, Chao et al. (1996) smoothed the vertical velocity four times by a Laplacian filter. In the present study, we use a nine-point smoothing algorithm. The horizontal smoothing operation does not change the integration of vertical transport. The domain-integrated vertical transport is derived from

$$V_{(z)} = \iint w_{(x,y,z)} dx dy. \quad (2)$$

### 3 Vertical velocity and transport in the thermocline

#### 3.1 Vertical transport

Influenced by wind stress at the sea surface and replenished

by overflow in the deep layer, marginal seas are likely of a vertical transport separated into upper and deep layers. For example, in the Banda Sea, a layer of minimum upward transport near 600 m separates upwelling within the thermocline from a deepwater upwelling pattern driven by the deep overflow in the Lifamatola Passage (Gordon et al., 2010). Based on the HYCOM GOFS3.1 reanalysis, we found that the time-mean domain-integrated vertical transport in the SCS can also be divided into two segments, in detail, a thermocline cell and a deepwater cell separated by a minimum vertical transport level at about 250 m depth. In the abyssal basin, the domain-integrated vertical transport  $V_{(z)}$  begins to increase upward from zero at 4 000 m to a maximum of  $1.5 \times 10^6 \text{ m}^3/\text{s}$  at about 1 500 m. Then, it decreases upward to a minimum layer of vertical transport at about 250 m. In the thermocline cell,  $V_{(z)}$  increases upward from 250 m to the other maximum of  $1.6 \times 10^6 \text{ m}^3/\text{s}$  at about 50 m before it decreases upward to zero at the sea surface (Fig. 4a). This two-segmented vertical transport is also derived from other independent reanalysis products. For example, the HYCOM GOFS3.0 reanalysis depicts two vertical cells of transport with a minimum vertical transport at about 600 m (Fig. 4c) while the SODA3.4.2 reanalysis shows a separating depth at the depth of 500 m (figure not shown). The depth of the maximum upward transport in the thermocline oc-

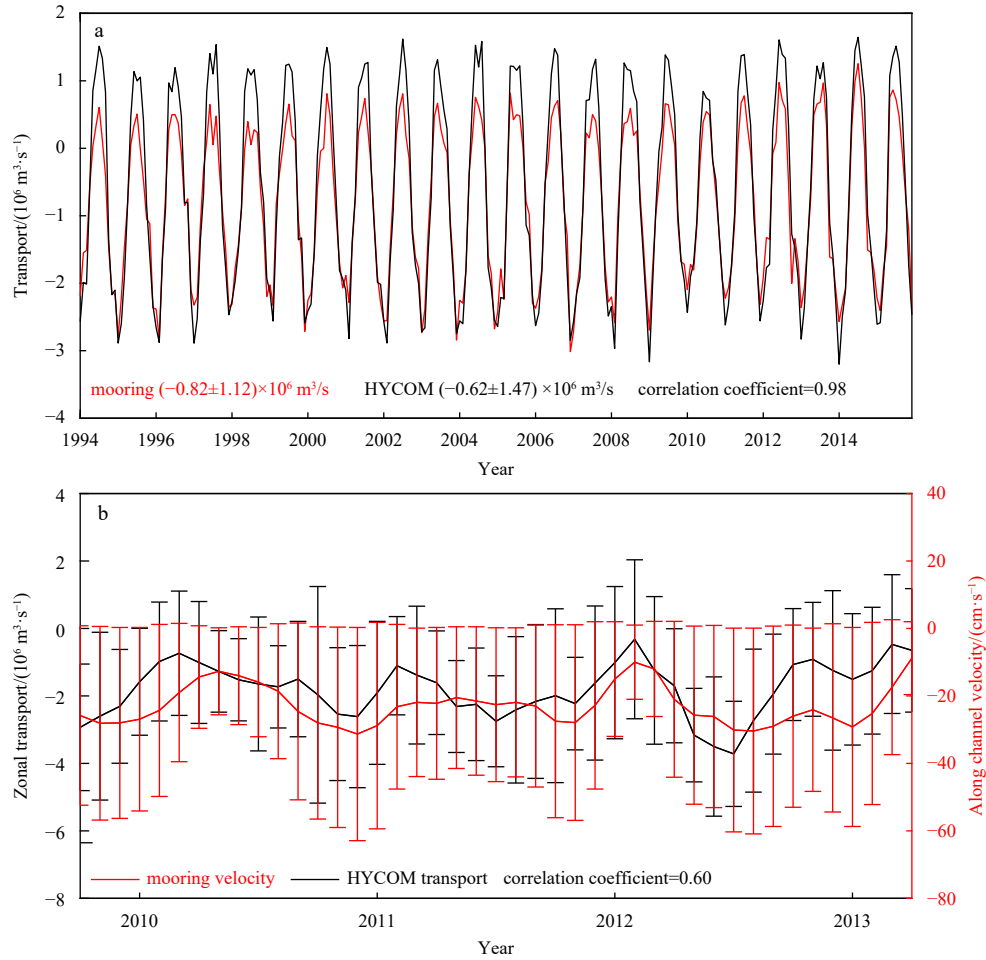


**Fig. 3.** Comparison of monthly mean transport from the HYCOM GOF3.1 reanalysis (black) with that from observations (red) in the Karimata Strait (a), and with along channel velocity (red) observed in the Luzon Trough (b). In a, positive transport is flow into the SCS and negative transport is flow into the Java Sea through the Karimata Strait. In b, negative velocity/transport indicates westward flow; bars indicate the standard deviations.

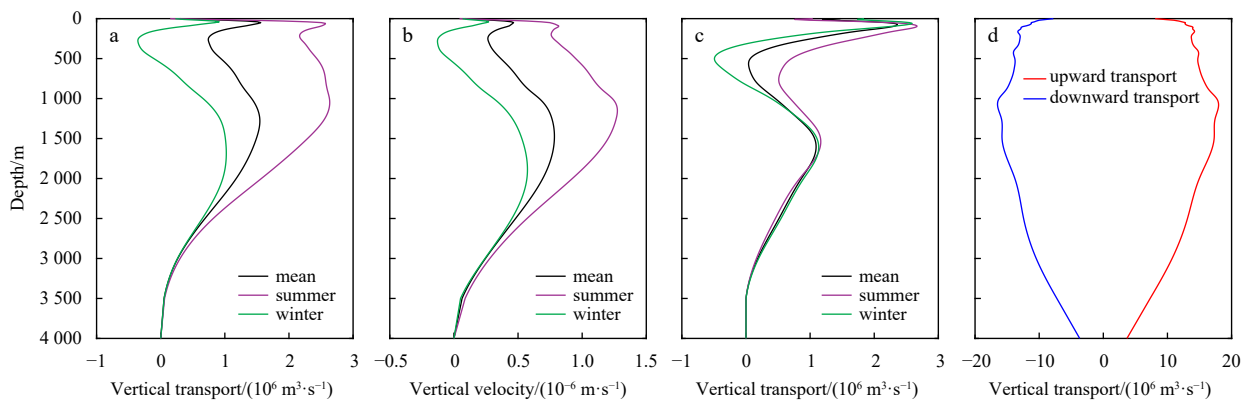


**Fig. 4.** Domain-integrated vertical transport (a) and domain-averaged vertical velocity (b) from the HYCOM GOF3.1 reanalysis; domain-integrated vertical transport from the HYCOM GOF3.0 reanalysis (c); separately integrated upward transport and downward transport from the HYCOM GOF3.1 reanalysis (d).

occurs at 50 m from the HYCOM GOF3.1 and SODA3.4.2 reanalysis, and about 60 m from the HYCOM GOF3.0 reanalysis. Although the minimum layer of the vertical transport may vary with models, the two-segmented feature is robust. In other words, a minimum layer of vertical transport occurs near the bottom of

the thermocline, and maximum transport occurs near the depth of Taiwan Strait sill and upper interface of the Luzon Strait overflow, respectively. Hereinafter, the distribution of vertical velocity and structure of vertical transport are derived from the HYCOM GOF3.1 reanalysis.

In the thermocline, the vertical transport varies with season due to the influence of monsoon. It manifests an upward section and a downward section in winter. Namely, the upward transport exists in the upper 150 m with its maximum occurring at 40 m, while the downward transport occurs between 150 m and 600 m with the downward maximum of  $-0.4 \times 10^6 \text{ m}^3/\text{s}$  at 250 m. In summer, the vertical transport maintains upward with its maximum of  $2.5 \times 10^6 \text{ m}^3/\text{s}$  at 60 m and minimum of  $2.2 \times 10^6 \text{ m}^3/\text{s}$  at about 250 m.

The vertical transport in the SCS is closely related to the flows between the SCS and adjacent seas. According to the numerical experiments carried out by Metzger and Hurlburt (1996) with a global model domain, the cyclonic circulation around the Philippines, which involves a westward flow in the Luzon Strait, a southward flow in the Sulu Archipelago, and an eastward flow in the Sulawesi Sea, is primarily a function of large-scale wind forcing over the Pacific Ocean and model geometry. This opinion was soon verified by Qu (2000), who applied Godfrey's (1989) "island rule" to the Philippines and interpreted Luzon Strait transport as a result of counterbalance between the basin-scale wind forcing over the Pacific Ocean and the friction created in the shallow passages that connect the SCS with its surrounding oceans. Further, Wang et al. (2006) used "island rule" to examine interannual variability of Luzon Strait transport and found that wind stress in the western and central equatorial Pacific Ocean is the key factor regulating the interannual variability of the Luzon Strait transport. Therefore, "island rule" is the primary forcing responsible for the Luzon Strait inflow and shallow-passage outflows. In addition, the local winds also play a nonnegligible role in volume fluxes through the shallow passages, by means of Ekman drift or Ekman transport. The total Ekman drift through all the straits is out from the SCS, in detail,  $0.3 \times 10^6 \text{ m}^3/\text{s}$ ,  $0.73 \times 10^6 \text{ m}^3/\text{s}$  and  $0.24 \times 10^6 \text{ m}^3/\text{s}$  in the time-mean, winter, and summer, respectively. Combined with both effects of remote wind forcing over the Pacific Ocean and local wind stress in the shallow passages, the total flow in the surface layer is out from the SCS (Table 1). As shown in Table 1, the net outflow in the upper 50 m is  $1.27 \times 10^6 \text{ m}^3/\text{s}$ ,  $0.79 \times 10^6 \text{ m}^3/\text{s}$ , and  $2.13 \times 10^6 \text{ m}^3/\text{s}$  in the time-mean, winter, and summer, respectively. In order to compensate the excessive outflow in the shallow depths, the subsurface water in the SCS has to be "pulled" upwards to maintain conservation of mass. Thus, the upward vertical transport in the thermocline is largely driven by the combination of the remote wind forcing over the Pacific Ocean and local wind stress in the straits, by means of "island rule" and the Ekman drift, respectively. The maximum vertical transport occurs approximately at 50 m, which is about the sill depth of the Karimata Strait and Taiwan Strait. Above this depth, the total outflow is contributed from the Mindoro Strait, Karimata Strait and Taiwan Strait, whereas below this depth, only the Mindoro Strait contributes and total outflow reduces.

### 3.2 Horizontal distribution of vertical velocity

In the SCS, the wind regime is controlled by the East Asian

monsoon with northeasterly wind in winter and southwesterly wind in summer. As a response to the local wind, the Ekman transport induced vertical velocity mainly exists on the continental shelves and is seasonal reversal. Downward velocity occurs in the western boundary of the SCS in winter and eastern boundary in summer and fall. Oppositely, upward velocity appears in the nearshore area west of Luzon Island in winter, and on the continental shelves off Vietnam and the southern China in spring and summer. As vertical velocity on continental shelves has been profoundly studied (Chai et al., 2001; Gan et al., 2013; Jing et al., 2015; Xie et al., 2012, 2017), hereinafter, the analysis is more focused on the vertical velocity in the deep SCS basin.

As the time-mean vertical transport reaches a maximum at 50 m and minimum at 250 m, the horizontal distribution of the time-mean vertical velocity at 50 m and 250 m is discussed in the following, representing vertical velocity at typical depths in the thermocline cell.

The time-mean wind stress curl over the SCS has a dipole pattern: anticyclonic curl in the north and cyclonic curl in the south, with the zero-wind stress curl line located from  $15^\circ\text{N}$ ,  $110^\circ\text{E}$  to  $20^\circ\text{N}$ ,  $120^\circ\text{E}$  (Qu, 2000). Accordingly, downward velocity at 50 m prevails on the north side of the zero-wind stress curl line (Fig. 5a), roughly along the 500 m isobath off the southern China. Upward velocities are found on both shoreward and seaward sides of this downward velocity band, roughly along the 100 m and 2 000 m isobaths, respectively, showing an alternating upward-downward band structure in the cross-shelf direction. This alternating upward-downward structure from the coast to deep waters was first proposed by Xie et al. (2017) and attributed to the alternating distribution of kinematic deformation, ageostrophic advection, and vertical mixing rate in the cross-shelf direction. Although the mechanism is derived from a diagnosis of three-dimensional vertical circulation in the upwelling and frontal zones on the continental shelf off China, the alternating band structure of the dynamic terms in the cross-shelf direction is apparently applicable to continental slopes and deep basin in the SCS.

Energetic upward velocity prevails to the west of Luzon Island (called the west Luzon eddy in Qu (2000) and Qu et al. (2007)) and is attributed to the strong positive wind stress curl there. Corresponding to the west Luzon eddy, a large cyclonic gyre is clearly seen in the horizontal current field (Fig. 5c). Upward velocity is remarkable east of Vietnam and north of Kalimantan due to the positive wind stress curl there. Generally, vertical velocity in the thermocline cell is stronger in the northern SCS than that in the southern SCS owing to the relatively strong wind stress curl and energetic entrainments and detrainments induced by the Kuroshio intrusion in the northern SCS.

At 250 m depth, although the domain-integrated vertical transport weakens, the vertical velocity is still energetic, reflecting strong entrainments and detrainments at this level. As we have estimated, both upward transport and downward transport reach up to  $13 \times 10^6 \text{ m}^3/\text{s}$ . This indicates that the entrainments and detrainments are greater than the net vertical transport at least by one order (Fig. 4d). Terrain dependent vertical velocity occurs along the continental shelf and slope due to the slope cur-

**Table 1.** Outflows in the upper 50 m (positive outward from the SCS, unit:  $10^6 \text{ m}^3/\text{s}$ )

	Luzon St.	Taiwan St.	Mindoro St.	Balabac St.	Karimata St.	Net outflow
Mean	-0.39 (-0.09)	1.25 (0.11)	0.09 (0.24)	-0.27 (0.04)	0.59	1.27 (0.3)
Winter	-1.81 (-0.54)	0.17 (0.47)	0.51 (0.96)	-0.42 (-0.16)	2.34	0.79 (0.73)
Summer	1.17 (0.20)	2.60 (-0.04)	-0.23 (-0.15)	-0.24 (0.23)	-1.17	2.13 (0.24)

Note: The numbers in brackets indicate contribution from the Ekman drift.

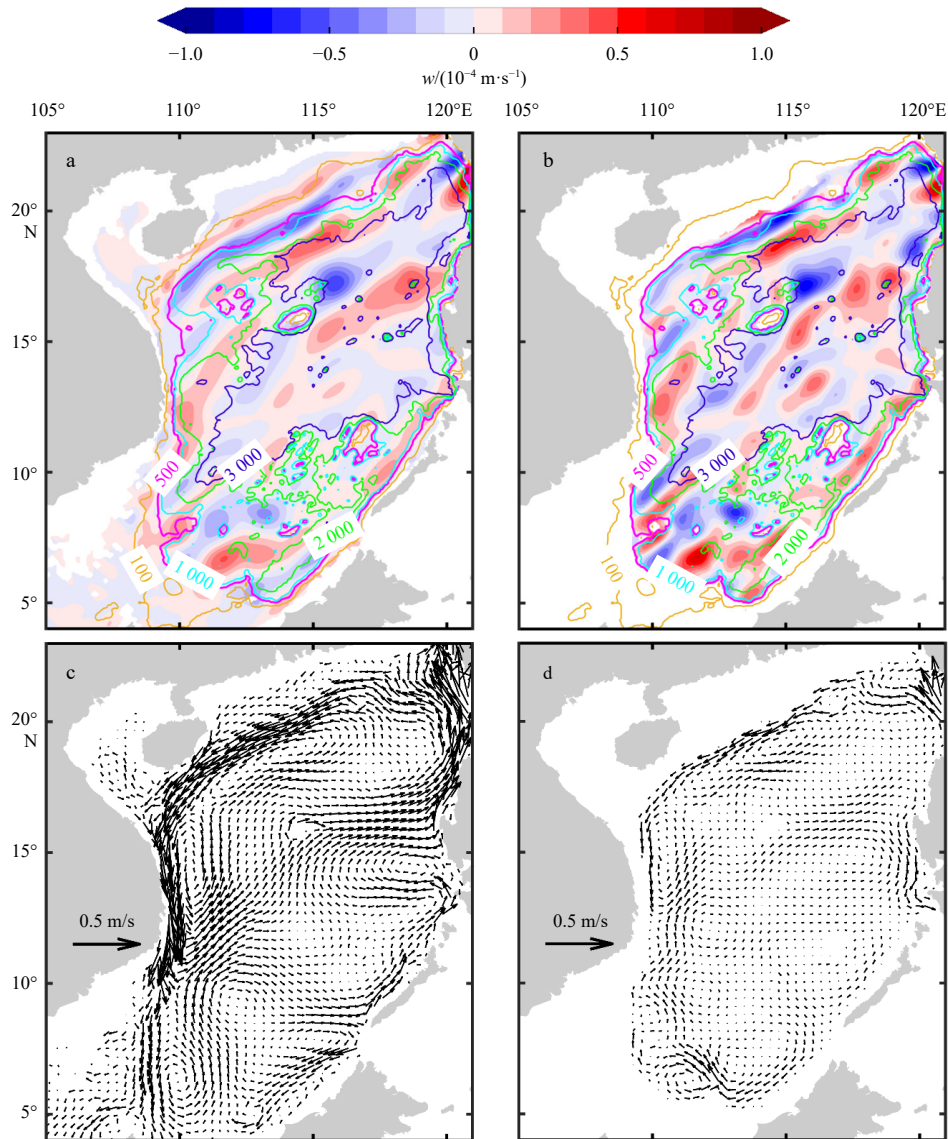


**Fig. 5.** Time-mean vertical velocity ( $w$ ) at 50 m (a), and 250 m (b), and time-mean horizontal velocity field at 50 m (c), and 250 m (d). The isobaths at 100 m, 500 m, 1 000 m, 2 000 m, and 3 000 m are indicated.

rent interacting with the meandering bottom topography (Figs 5a, b). When the bottom currents encounter a convex/concave slope, the upslope/downslope velocity generates (Gan and Allen, 2002; Song and Chao, 2004; Cai and Gan, 2020). The upwelling zone occurs near 13°N east of Vietnam and corresponds to an eastward offshore jet which can be seen from the horizontal velocity field (Fig. 5d). Upwelling there is a compensation to the eastward volume transport. The aforementioned alternating upward-downward band structure in the cross-shelf direction is clearly shown on the horizontal plane (Fig. 5b) and vertical transects (Fig. 6).

Monsoon induced vertical velocity experiences a seasonal reversal, particularly in the nearshore areas. In winter, the zero-wind stress curl line is roughly located from 5°N, 105°E to 20°N, 120°E with positive values in the south and negative ones in the north. As a result, at 50 m depth, strong downward velocity band appears on the north side of the 500 m isobath off the southern China (Fig. 7a). Upwelling west of Luzon Island corresponds to the local cyclonic wind stress curl, while downward velocity east

of Vietnam is attributed to the resultant of the downward Ekman pumping and onshore Ekman transport. At 250 m, the Ekman transport induced downward velocity nearly vanishes along the northern slope and western boundary (Fig. 7b). Vertical velocity can be identified over a dramatically changing topography, for instance, along Vietnam coast. When the WBC flows southward to 13°N along Vietnam coast, the water depth becomes deeper. According to conservation of potential vorticity, i.e.,  $f + \zeta/h = \text{constant}$ , a positive relative vorticity forms accompanying with upwelling. When the WBC flows further southward to 10°N, the water depth becomes shallower. Accordingly, a negative relative vorticity generates accompanying with downwelling below the 200 m depth (Fig. 7b).

In summer, as a response to the southwesterly monsoon, the Ekman transport induced nearshore upward velocities intensify along the continental shelves off Vietnam and the southern China (Fig. 7c). Under the effect of local wind stress and shelf topography, a northward WBC and a southward WBC converge and form a strong offshore current near 13°N east of Vietnam.

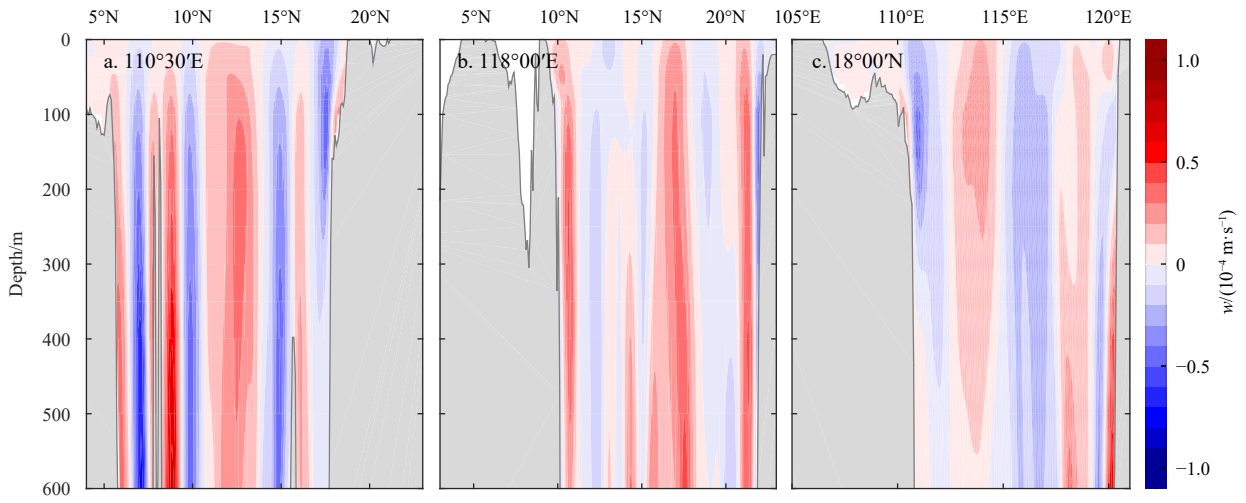


**Fig. 6.** Alternating bands of the upward-downward velocity ( $w$ ) seen from vertical sections in the thermocline cell.

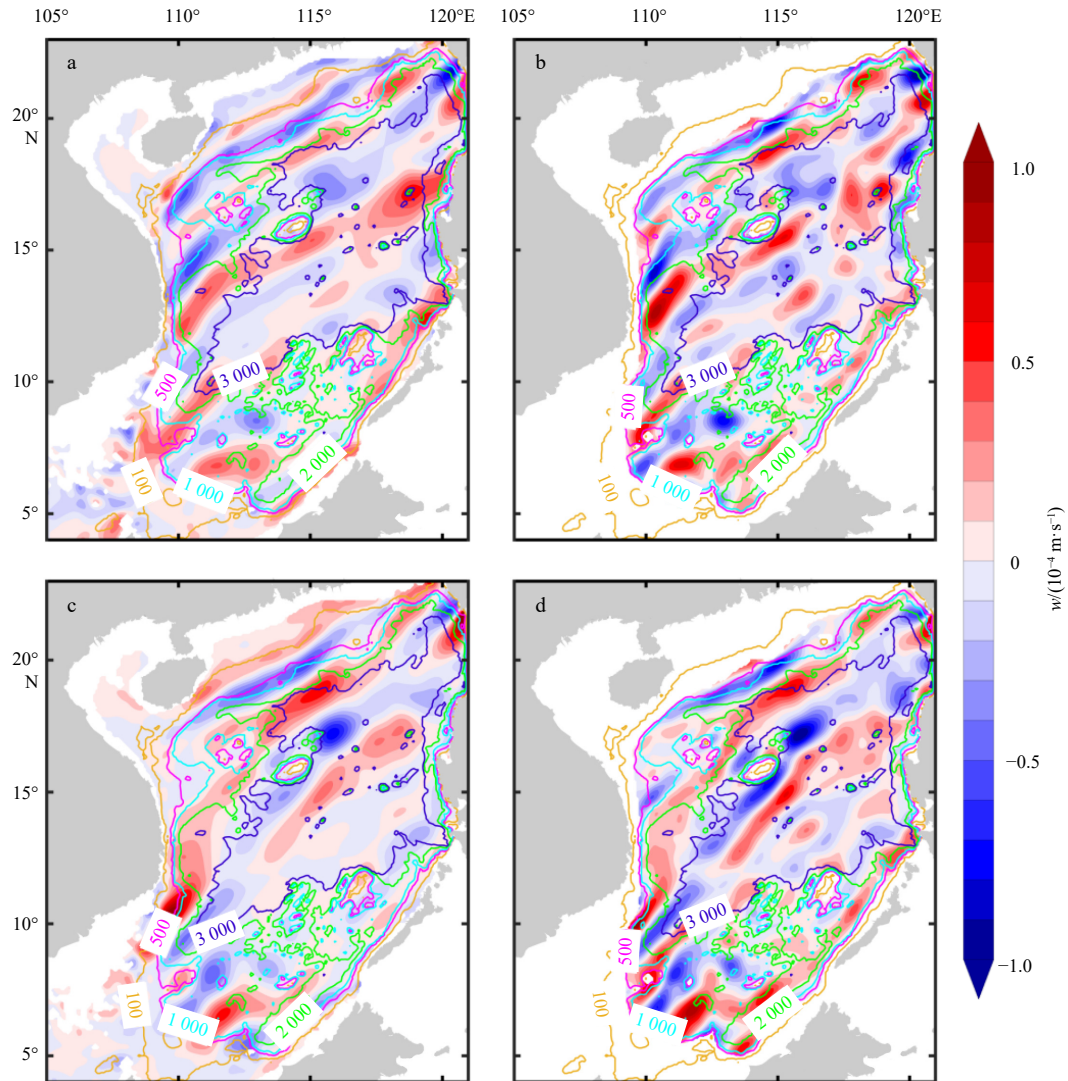


**Fig. 7.** Vertical velocity ( $w$ ) at 50 m (a), and 250 m (b) in winter, and at 50 m (c), and 250 m (d) in summer. The isobaths at 100 m, 500 m, 1 000 m, 2 000 m, and 3 000 m are indicated.

Upwelling in the vicinity has been reported in literature (Shaw and Chao, 1994; Chu et al., 1998; Gan et al., 2006; Fang et al., 2012) and is attributed to the vertical compensation to the volume loss of offshore transport (Fig. 7d).

#### 4 Vertical velocity and transport in the deepwater cell

##### 4.1 Vertical transport

Below the thermocline, the upward transport strengthens with depth and reaches the other maximum at about 1 500 m. This depth coincides with the aforementioned upper interface of the Luzon Strait deepwater overflow, under which the cold and dense Pacific water impinges into the SCS through the Luzon Strait (Qu et al., 2006; Zhu et al., 2017b). The density of the Luzon Strait overflow reaches up to  $36.88\sigma_2$  (Zhao et al., 2014) or  $27.68\sigma_\theta$  (Zhu et al., 2017b) in the Luzon Trough, greater than the maximum density  $27.66\sigma_\theta$  of the SCS near bottom water. Majority of the overflow sinks to the abyssal basin and in turn pushes the abyssal water upwards to fulfill a renewal process. Thus, the mechanism of vertical transport in the deep cell differs from that in the thermocline. Namely, the deep water is “pushed” upward by the dense Luzon Strait overflow from the bottom whereas the subsurface water is “pulled” upward by the remote wind forcing through “island rule” and local wind forcing. The vertical transport of  $1.5\times 10^6$  m<sup>3</sup>/s at 1 500 m coincides with the volume flux in

the Luzon Strait below 1 500 m, implying that the upwelling pattern in the deep SCS basin is driven by the Luzon Strait overflow. The time-mean overflow transport below 1 500 m from the HYCOM reanalysis shows good agreement with the observations, specifically,  $1.5\times 10^6$  m<sup>3</sup>/s in a two-week observation (Zhao et al., 2014) and  $(0.88\pm 0.77)\times 10^6$  m<sup>3</sup>/s in a 3.5-year of continuous mooring observation (Zhou et al., 2014).

##### 4.2 Horizontal distribution of vertical velocity

As the domain-integrated vertical transport in the deepwater cell varies less significant with season, thus, it is considered “steady” in this study. Only the time-mean vertical velocity and transport are discussed in the following albeit seasonal change in vertical velocity still exists. Figure 8 depicts the vertical velocity at 1 500 m, representing the depth above the Luzon Strait overflow, and at 2 500 m, indicative of the depths below the Luzon Strait sill, respectively. In the deep SCS basin, downward vertical velocity primarily appears near the gaps in the Heng-Chun Ridge shown in Fig. 1 and on the shoreward side of the 3 000 m isobath. The upward velocity occurs to the west side of the aforemen-

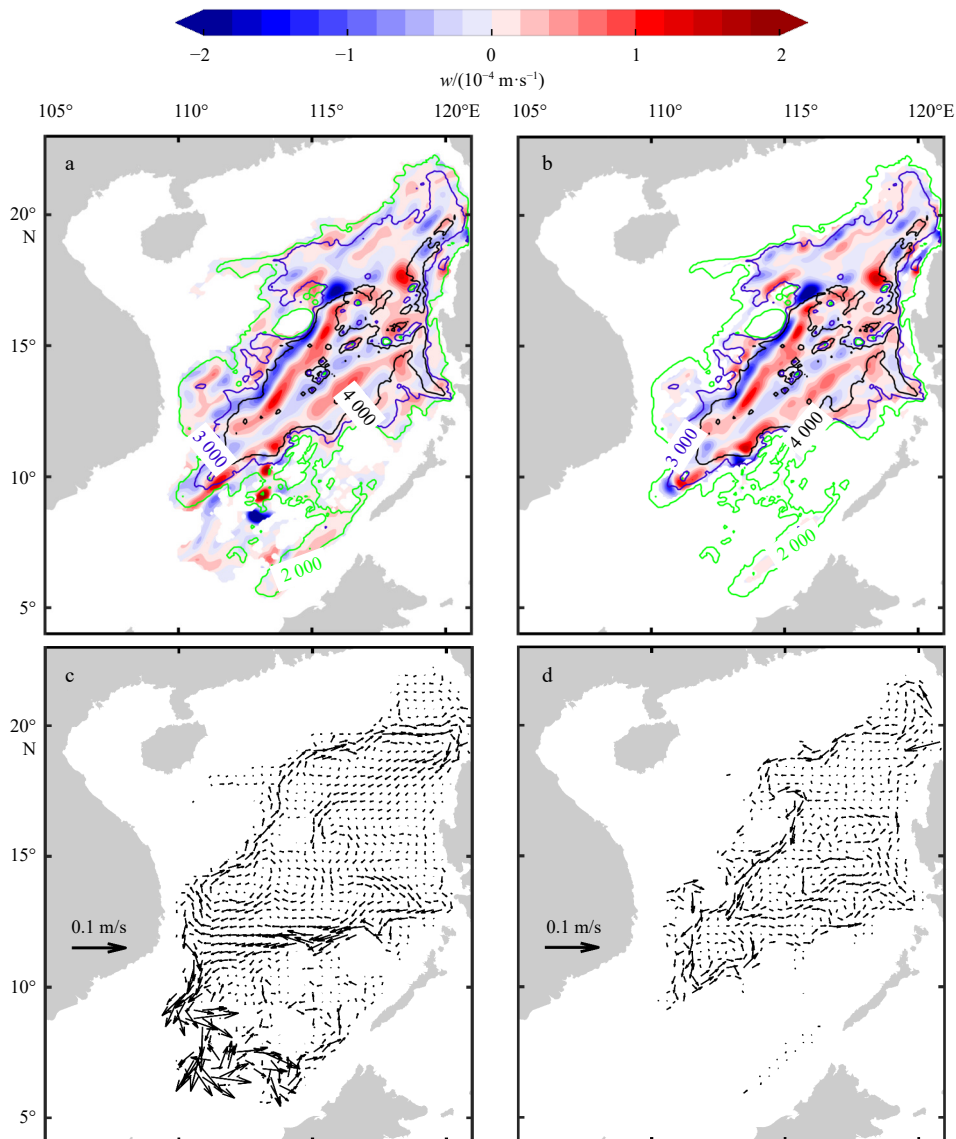


Fig. 8. Time-mean vertical velocity ( $w$ ) at 1 500 m (a), and 2 500 m (b), and associated horizontal velocity field in c and d. The isobaths at 2 000 m, 3 000 m, and 4 000 m are indicated.

tioned downwelling near the Heng-Chun gaps; at the northern and southern ends of the abyssal basin below 3 000 m (hereinafter, the northern end and southern end); on the seaward side of the 3 000 m isobath, as well as around the Nansha Islands. Among them, the upwelling sites around the southern and northern ends were identified as the main sites of deep water ventilation in [Chao et al. \(1996\)](#).

The Luzon Strait deepwater overflow carries the cold and dense Pacific water and sinks mainly through two gaps in the Heng-Chun Ridge. After the overflow sinks into the abyssal Manila Trench leaning the steep slope, it drives a compensatory upwelling on the west side and a northeastward flow along the Manila Trench. Strong downwelling and upwelling sites west of the gaps are reproduced by the HYCOM GOFS3.1 reanalysis ([Fig. 8b](#)). As the slope is very steep west of the Luzon Strait, the downwelling and upwelling juxtapose closely on both sides of the 3 000 m isobath. The upwelling weakens upward by spreading around ([Fig. 8a](#)). The upwelling around the northern end seems to be topographically lifted. When the overflow leaves the Manila Trench, it turns to the northern end along a northward trough. As water depth at the northern end is greater than the depth in the east, north and west, the northward current consequentially divides into an upslope current by orographic lifting and a cyclonic flow around the northern end ([Fig. 8d](#)). The former forms an upwelling source associated with the Luzon Strait overflow while the latter becomes a boundary current off the southern China. The upwelling around the northern end is accordant with the early finding observed by [Wang \(1986\)](#) and simulated by [Chao et al. \(1996\)](#) and called southwest of Taiwan upwelling. Thus, the present study provides additional evidence on the existence of upwelling southwest of Taiwan. As the Luzon Strait overflow is strong and all year round, the upwelling around the northern end is persistent and able to extend to shallow depths.

One of the most remarkable features in the deep cell is upward velocity enhances on the seaward side of the 3 000 m

isobath ([Fig. 9](#)), consistent with the rising sites from a backward integration of Lagrangian trajectories in [Shu et al. \(2014\)](#). As a result, the locally integrated vertical transport on the seaward side of the 3 000 m isobath accounts for the majority of the domain-integrated transport in the deep layer ([Table 2](#)). At 2 500 m, the locally integrated vertical transport on the seaward side of the 3 000 m isobath is much greater than the domain-integrated vertical transport, indicating dominant upward (downward) transport on the seaward (shoreward) side of the 3 000 m isobath. At shallower depths, the integrated vertical transport on the seaward side of the 3 000 m isobath is negative, indicative of downward transport in the central deep basin and prevailing upward transport on the continental shelves, as shown at 500 m.

Upwelling near the southern end is a prominent feature of the deep water ventilation, which was also simulated by [Chao et al. \(1996\)](#) as one of the major renewal sites of the abyssal water (named upwelling southeast of Vietnam). The upwelling sites around the southern end correspond to the cyclonic eddies there, indicating a possible mechanism related with eddy dynamics ([Fig. 8c](#)). Besides, upward velocities are found around the Nansha Islands, where coral reefs, atolls and banks rising steeply from the seabed can enhance vertical mixing and result in orographic lifting of bottom currents. In the central abyssal basin, a northeast-southwest downward velocity band along the 4 000 m isobath and an upward velocity band on the seaward side of it are presented in [Fig. 8](#). This feature has not been reported by either observations or numerical simulations. The authenticity needs to be confirmed by observations.

## 5 Discussion

### 5.1 A possible mechanism for deepwater upwelling

In this section, we focus on elaborating why upward velocity arise from the steep slope, and then propose a possible mechanism for deepwater upwelling. When [Xie et al. \(2013\)](#) examined

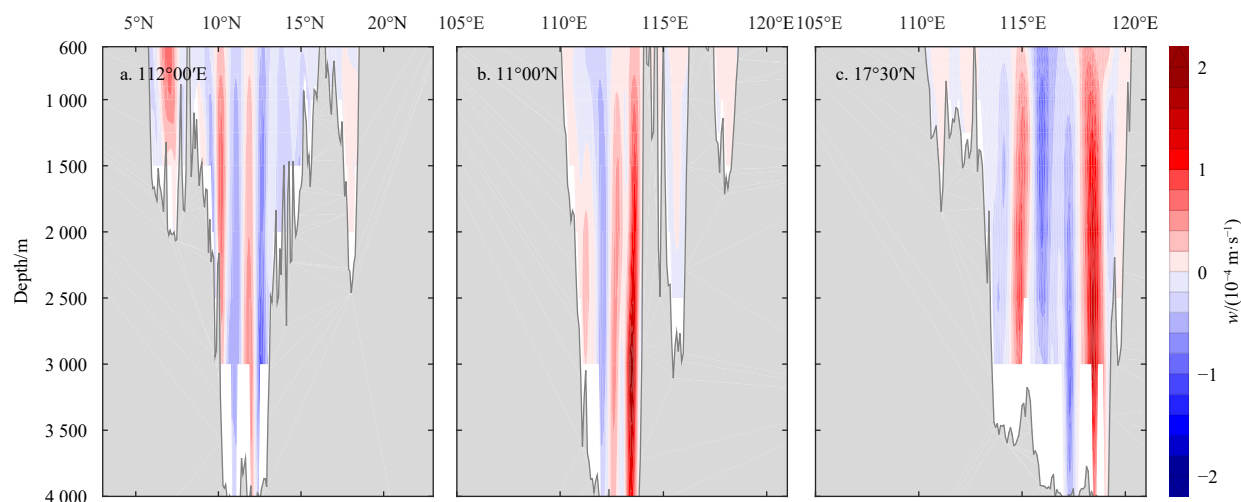


**Fig. 9.** Upward vertical velocity ( $w$ ) generates on the seaward side of the 3 000 m isobath along transect to the southeast of Vietnam (a), on the southern slope (b), west of the Heng-Chun Ridge (c).

**Table 2.** Comparison of vertical transport on the seaward side of the 3 000 m isobath with the domain-integrated transport at different vertical levels (unit:  $10^6 \text{ m}^3/\text{s}$ )

	100 m	500 m	1 500 m	2 500 m
Seaward side of 3 000 m	0.19	-0.42	1.13	1.97
Domain-integrated	1.25	0.94	1.49	0.69

the relationship between model topography and deep-layer SCS circulation using depth-averaged linear shallow water momentum equations, the current velocity  $\vec{V}$  in deep basin is derived to be proportional to the gradient of water depth  $\nabla H$  and inversely proportional to  $H^2$ , i.e.,  $|\vec{V}| \propto |\nabla H|/H^2$ . In the meantime, according to vortex balance, we have equation  $f \cdot dw/dz = \beta v$ , where  $f$  is the velocity Coriolis parameter,  $z$  is the vertical coordinate,  $w$  and  $v$  are the vertical velocity and meridional velocity. Along the western boundary of the SCS,  $\vec{V}$  is largely meridional and can be approximated by  $v$ , so the vertical vortex stretching meets

$$\frac{dw}{dz} \propto \frac{\beta}{f} |\nabla H|/H^2. \quad (3)$$

Considering vertical velocity is zero at locally flat ocean floor, the vertical velocity becomes

$$w_{(z)} \propto \int_{-H}^z \frac{\beta}{f} |\nabla H|/H^2 dz. \quad (4)$$

This implies that the greater where the depth gradient is, the greater the vertical velocity above the basin floor. In the SCS, the greatest depth gradient occurs off the continental slope or along the rim of the abyssal basin, where the 3 000 m and 4 000 m isobaths are only 30–40 km apart. As seen in Fig. 9, strong upward velocity occurs along the slope margin, in particular, on the seaward side of the 3 000 m isobath.

To validate Eq. (4), we depict  $\frac{\beta}{f} |\nabla H|/H^2$  in Fig. 10. The function  $\frac{\beta}{f} |\nabla H|/H^2$  is not vertical velocity, but to be integrated for vertical velocity. So, it represents the distribution of the vertical velocity. To better compare the effect of topography on the distribution of vertical velocity, two different topographies are employed, i.e., the HYCOM model topography and ETOPO5. The former is of a coarser resolution than the latter. Figure 10 shows that in both cases, the vertical velocity strengthens with topography gradient, in particular, in the vicinity of the 3 000 m and

4 000 m isobaths. The difference is also obvious that the vertical velocity in the HYCOM topography is largely weakened on a relatively smooth floor where the bottom is flattened in model grid and impermeable bottom boundary condition is applied in the model.

As Eq. (4) is derived from depth-averaged linear shallow water momentum equations to examine the relationship between model topography and vertical velocity, the pattern in Fig. 10 differs from the vertical velocity in Fig. 8 in detail. It is understandable that Fig. 8 is simulated by a comprehensive ocean model and thus contains characteristic of Fig. 10, but not limited to that.

Further, we establish a simple model for deepwater upwelling above steep slopes. Assuming the thickness of bottom layer is  $h_0$ , bottom friction cannot be ignored in this layer. In a sense of liner dynamics, if the  $y$ -axis is set alongshore (i.e., north-eastward) and the  $x$ -axis perpendicular to the  $y$ -axis and off the continental slope (i.e., seaward), we add a bottom friction term to the geostrophic equations in the bottom layer,

$$f v_b - \frac{1}{\rho} \frac{\partial P_b}{\partial x} + \frac{\tau_{bx}}{\rho h_0} = 0, \quad (5)$$

$$-f u_b - \frac{1}{\rho} \frac{\partial P_b}{\partial y} + \frac{\tau_{by}}{\rho h_0} = 0, \quad (6)$$

where  $\tau_{bx}$  and  $\tau_{by}$  are the bottom friction terms. Assuming water flows alongshore, both observations and numerical simulations manifest that the alongshore velocity is much larger than the offshore velocity, approximately by one order. Accordingly, the offshore pressure gradient force is much larger than the alongshore pressure gradient force, i.e.,  $\frac{1}{\rho} \frac{\partial P_b}{\partial y}$  and  $u_b$  are much smaller than  $\frac{1}{\rho} \frac{\partial P_b}{\partial x}$  and  $v_b$ , respectively. When the bottom friction is superimposed on the alongshore flow above the steep slope, the geostrophic balance is no longer valid. To examine the effect of the bottom friction on the alongshore flow, we temporarily put aside the alongshore pressure gradient force, and focus on the relationship between the Coriolis force and friction. In  $y$ -direction, if  $\frac{1}{\rho} \frac{\partial P_b}{\partial y}$  is ignored in Eq. (6), thus,

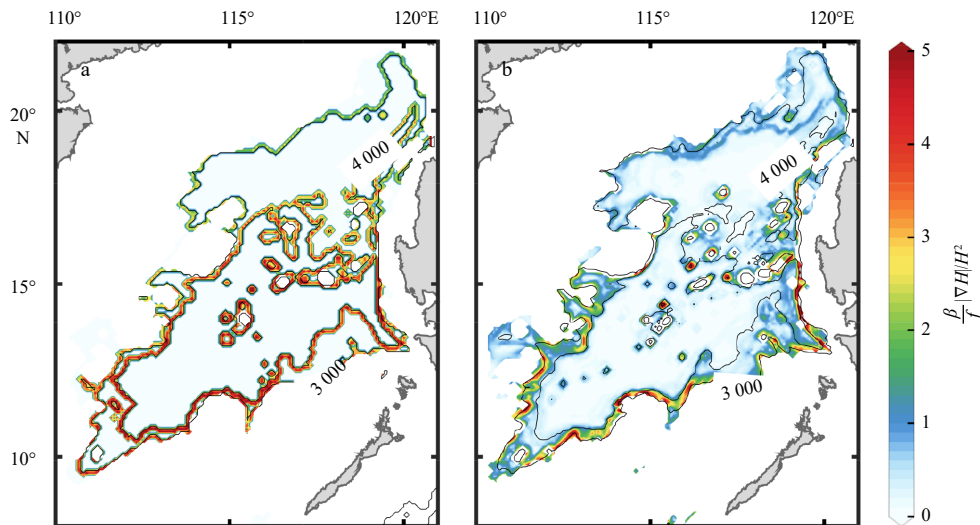


Fig. 10. Distribution of  $\frac{\beta}{f} |\nabla H|/H^2$  derived from the HYCOM model topography (a), and ETOPO5 (b). The isobaths at 3 000 m and 4 000 m are indicated.

$$fu_b \approx \frac{\tau_{by}}{\rho h_0}. \quad (7)$$

When a linear friction is applied in Eq. (7),  $\tau_{by} = \rho R v_b$ , then

$$u_b \approx \frac{R}{f h_0} v_b, \quad (8)$$

where  $R$  is a linear drag coefficient about  $1 \times 10^{-4}$ ,  $f$  is the Coriolis parameter about  $1 \times 10^{-4} \text{ s}^{-1}$ ,  $h_0$  is the bottom layer thickness about  $1 \times 10^2 \text{ m}$ . Along the western boundary slope, the typical magnitude of  $v_b$  is  $-1 \times 10^{-2} \text{ m/s}$  (i.e., southwestward), then  $u_b \approx 1 \times 10^{-2} v_b = -1 \times 10^{-4} \text{ m/s}$ . The negative sign of  $u_b$  represents toward the continental slope (onshore). This suggests that due to the bottom friction superimposed on the alongshore flow immediately above the steep slope, the geostrophic balance is no longer valid. As a result, a shoreward component of bottom current generates and turns to be upslope current. Although the across-isobath component accounts for only 1% of magnitude of the alongshore DWBC, it crucially converts kinetic energy from horizontal circulation to potential energy and generates upward vertical velocity (Xiao et al., 2013).

When a quadric friction term is applied in Eq. (7), i.e.,  $\tau_{by} = \rho C_D v_b |v_b|$ , then

$$u_b \approx \frac{C_D}{f h_0} v_b |v_b|, \quad (9)$$

where  $C_D$  is a quadric drag coefficient about  $1 \times 10^{-3}$ . In the case of  $v_b = -1 \times 10^{-2} \text{ m/s}$ ,  $u_b$  can be estimated:  $u_b \approx 1 \times 10^{-1} v_b |v_b| \approx -1 \times 10^{-5} \text{ m/s}$ . So, the similar conclusion is approached to that of linear friction, i.e., a small onshore velocity component generates above the steep slopes and turns to be an upward motion. The result of the qualitative analysis from our simplified concept is consistent with previous studies (Xiao et al., 2013).

In Fig. 8, some upward and downward velocities occur next to each other, which cannot be explained by the onshore motion

only. Thus, the onshore motion we proposed is only one of the possible mechanisms. Moreover, the occurrence of alternating striations in the spatial pattern of vertical velocity seems related with second-order circulation and complicated interaction between slope current and bottom topography. At this stage, we leave it as an open issue for further studies.

### 5.2 The role of vertical velocity and transport in the SCS circulation

Although the vertical velocity is related with local dynamic processes and vertical transport is related with volume budget, both of them act as a bridge connecting circulation in the horizontal layers and play an important role in the horizontal and vertical circulation in the SCS. The time-mean meridional overturning streamfunction derived from the HYCOM reanalysis includes a positive meridional overturning circulation (MOC) (defined as a southward transport in the lower limb, upward transport in the south and northward transport in the upper limb) in the upper and deep layers, and a negative MOC (defined opposite to the positive MOC) at the middle depths. This sandwiched MOC structure in vertical was first proposed with HYCOM GOFS3.0 reanalysis (Shu et al., 2014), which is basically consistent with the vertical streamfunction from other model outputs, e.g., the SODA, BRAN and JPL-R (Xie et al., 2013; Zhu et al., 2016). To show the connection between the vertical transport and MOC in the SCS, the time-mean vertical transport in Fig. 4a is redrawn with vertical hollow arrows in Fig. 11. The upward vertical transport, along with the southward Luzon Strait deepwater overflow (i.e., the lower limb) and northward intermediate water (i.e., outward flow to the western Pacific), forms a positive MOC in the deep SCS basin. Apparently, the vertical transport plays a role of vertical limb in the SCS MOC.

In large-scale dynamical processes, vortex stretching is balanced by the advection of the background potential vorticity. This may give a direct interpretation of the sandwiched horizontal circulation in the SCS, including a cyclonic circulation in the upper and deep layers, and an anticyclonic circulation in the middle layer (Yuan, 2002; Xu and Oey, 2014; Gan et al., 2016; Zhu

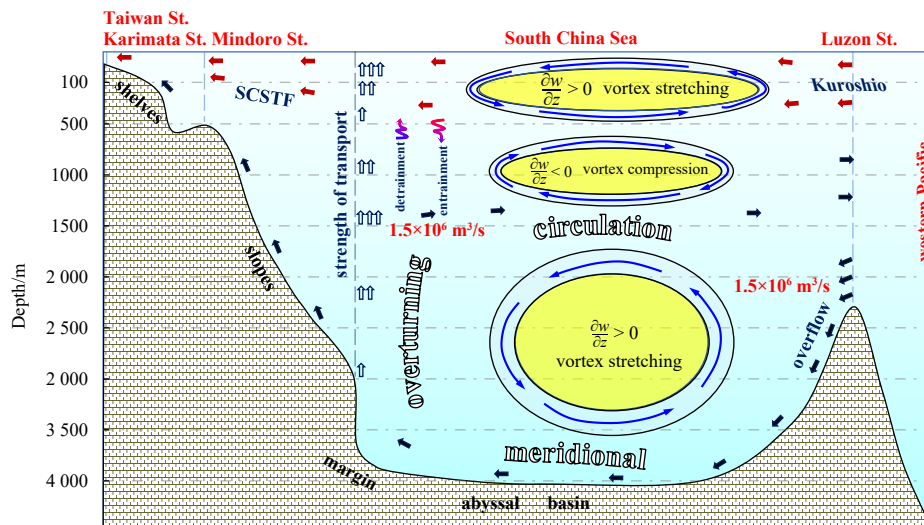


**Fig. 11.** The role of vertical transport in the three-dimensional SCS circulation. Dark blue and red arrows indicate the Luzon Strait overflow and Kuroshio intrusion, respectively. The hollow arrows in vertical present the strength of domain-averaged vertical velocity, inferring a positive vertical gradient of vertical velocity in the upper and deep layer, and a negative one in the intermediate layer. The thin blue arrows encompassing the yellow planes denote the direction of layer-averaged horizontal circulation in the basin scale. The abbreviation SCSTF indicates South China Sea throughflow.

et al., 2017a). The formation mechanism was mainly attributed to the sandwiched lateral potential vorticity flux through the Luzon Strait (Gan et al., 2016; Zhu et al., 2017a). As shown in Fig. 4b, the domain-averaged vertical velocity increases upward from zero at 4 000 m to its maximum of  $0.75 \times 10^{-6}$  m/s at about 1 500 m; it decreases upward between 250 m and 1 500 m and increases upward again from  $0.3 \times 10^{-6}$  m/s at 250 m to the maximum of  $0.5 \times 10^{-6}$  m/s at 50 m. This vertical change of the domain-averaged vertical velocity is schematically diagrammed by the hollow arrows in Fig. 11, in which the greater the number of the hollow arrows, the stronger the domain-averaged upward velocity. Apparently, the vertical gradient of vertical velocity is positive, i.e.,  $dw/dz > 0$  in the upper 250 m and below 1 500 m. This yields a vortex stretching and accordingly an increasing layer thickness  $h$  in the upper and deep layers. According to conservation of potential vorticity,  $f + \zeta/h = \text{constant}$ , the domain- and layer-averaged relative vorticity  $\zeta$  must increase. As a result, the layer-averaged circulation tends to be cyclonic in both upper and deep layers. In contrast, between the 250 m and 1 500 m depths, the vertical gradient of vertical velocity is negative, i.e.,  $dw/dz < 0$ . Therefore, it yields a vortex compression and a decreasing layer thickness  $h$ , which induces a negative domain- and layer-averaged  $\zeta$ , consequently results in a layer-averaged anticyclonic circulation at the middle depths. From this point of view, the vertical gradient of the domain-averaged vertical velocity regulates the sandwiched circulation in the SCS.

## 6 Summary and conclusions

A robust two-segmented vertical transport in the SCS was revealed based on the HYCOM GOF3.1 reanalysis and other independent reanalysis products. A layer of minimum vertical transport separates the thermocline cell from the deepwater cell. We expect this work, with the first picture of the two-segmented vertical transport, will offer some insights to the understanding of the vertical transport in the SCS. We suggest that the two-segmented vertical transport may be applicable to marginal seas where the upwelling pattern is forced by wind stress curl at the sea surface and by overflow in the deep layer.

In the thermocline cell, the time-mean vertical transport reaches a maximum approximately at the sill depth of Taiwan Strait and Karimata Strait. The upward transport is primarily ascribed to the “island rule” by remote winds over the Pacific Ocean and local Ekman drift in the shallow passages, which force excessive water out of the SCS in the surface layer. As a result, the subsurface water in the SCS is pulled upward to compensate the volume loss. Strong vertical velocities are mainly distributed in the northern SCS, in alternating upward-downward velocity bands from coast to deep basin.

In the deepwater cell, the time-mean upward transport reaches a maximum of  $1.5 \times 10^6$  m<sup>3</sup>/s at about 1 500 m, accordant with the Luzon Strait overflow in transport rate and upper interface in depth, indicative of the upward “push” of the dense Luzon Strait overflow in the deepwater renewal process. Onshore currents are derived from the alongshore DWBC with bottom friction, generating upward vertical velocity off the steep slope breaks. This conception may also be applicable to marginal seas where deep boundary circulation is driven by a deepwater overflow.

The vertical velocity and transport play an important role in connecting the horizontal and vertical circulation in the SCS. On one hand, the vertical velocity acts as the vertical limb of the SCS MOC. On the other hand, the vertical gradient of domain-aver-

aged vertical velocity regulates the horizontal circulation in the SCS. In the upper and deep layers, the positive gradient of the vertical velocity yields a vortex stretching and layer-averaged cyclonic circulation. In contrast, the negative gradient of the vertical velocity yields a vortex compression and layer-averaged anticyclonic circulation at middle depths.

## Acknowledgements

The monthly mean series of along channel velocity in Fig. 3b is kindly provided by Chun Zhou (personal communication).

## References

- Cai Zhongya, Gan Jianping. 2020. Dynamics of the cross-layer exchange for the layered circulation in the South China Sea. *Journal of Geophysical Research: Oceans*, 125(8): e2020JC016131, doi: [10.1029/2020JC016131](https://doi.org/10.1029/2020JC016131)
- Chai Fei, Xue Huijie, Shi Maochong. 2001. Formation and distribution of upwelling and downwelling in the South China Sea. *China Oceanography Symposium*, 13: 117–128
- Chao S Y, Shaw P T, Wu S Y. 1996. Deep water ventilation in the South China Sea. *Deep-Sea Research Part I: Oceanographic Research Papers*, 43(4): 445–466, doi: [10.1016/0967-0637\(96\)00025-8](https://doi.org/10.1016/0967-0637(96)00025-8)
- Chu P C, Chen Yuchun, Lu Shihua. 1998. Wind-driven South China Sea deep basin warm-core/cool-core eddies. *Journal of Oceanography*, 54(4): 347–360, doi: [10.1007/BF02742619](https://doi.org/10.1007/BF02742619)
- Fang Guohong, Wang Gang, Fang Yue, et al. 2012. A review on the South China Sea western boundary current. *Acta Oceanologica Sinica*, 31(5): 1–10, doi: [10.1007/s13131-012-0231-y](https://doi.org/10.1007/s13131-012-0231-y)
- Gan Jianping, Allen J S. 2002. A modeling study of shelf circulation off northern California in the region of the Coastal Ocean Dynamics Experiment 2. Response to relaxation of upwelling winds. *Journal of Geophysical Research: Oceans*, 107(C11): 3184, doi: [10.1029/2001JC001190](https://doi.org/10.1029/2001JC001190)
- Gan Jianping, Ho H S, Liang Linlin. 2013. Dynamics of intensified downwelling circulation over a widened shelf in the Northeastern South China Sea. *Journal of Physical Oceanography*, 43(1): 80–94, doi: [10.1175/JPO-D-12-02.1](https://doi.org/10.1175/JPO-D-12-02.1)
- Gan Jianping, Li H, Curchitser E N, et al. 2006. Modeling South China Sea circulation: Response to seasonal forcing regimes. *Journal of Geophysical Research: Oceans*, 111(C6): C06034, doi: [10.1029/2005JC003298](https://doi.org/10.1029/2005JC003298)
- Gan Jianping, Liu Zhiqiang, Hui C R. 2016. A three-layer alternating spinning circulation in the South China Sea. *Journal of Physical Oceanography*, 46(8): 2309–2315, doi: [10.1175/JPO-D-16-0044.1](https://doi.org/10.1175/JPO-D-16-0044.1)
- Godfrey, J S. 1989. A Sverdrup model of the depth-integrated flow for the world ocean allowing for island circulations. *Geophysical & Astrophysical Fluid Dynamics*, 45(1–2): 89–112
- Gordon A L, Sprintall J, Van Aken H M, et al. 2010. The Indonesian throughflow during 2004–2006 as observed by the INSTANT program. *Dynamics of Atmospheres and Oceans*, 50(2): 115–128, doi: [10.1016/j.dynatmoce.2009.12.002](https://doi.org/10.1016/j.dynatmoce.2009.12.002)
- Jing Zhiyou, Qi Yiquan, Du Yan, et al. 2015. Summer upwelling and thermal fronts in the northwestern South China Sea: Observational analysis of two mesoscale mapping surveys. *Journal of Geophysical Research: Oceans*, 120(3): 1993–2006, doi: [10.1002/.2014JC010601](https://doi.org/10.1002/.2014JC010601)
- Li Li, Qu Tangdong. 2006. Thermohaline circulation in the deep South China Sea basin inferred from oxygen distributions. *Journal of Geophysical Research: Oceans*, 111(C5): C05017, doi: [10.1029/2005JC003164](https://doi.org/10.1029/2005JC003164)
- Metzger E J, Hurlburt H E. 1996. Coupled dynamics of the South China Sea, the Sulu Sea, and the Pacific Ocean. *Journal of Geophysical Research: Oceans*, 101(C5): 12331–12352
- Nitani H. 1972. Beginning of the Kuroshio. In: Stommel H, Yashida K, eds. *Kuroshio: Physical Aspects of the Japan Current*. Seattle, WA, USA: University of Washington Press, 129–163
- Qu Tangdong. 2000. Upper-layer circulation in the South China Sea. *Journal of Physical Oceanography*, 30(6): 1450–1460, doi:

[10.1175/1520-0485\(2000\)030<1450:ULCITS>2.0.CO;2](https://doi.org/10.1175/1520-0485(2000)030<1450:ULCITS>2.0.CO;2)

- Qu Tangdong, Du Yan, Gan Jianping, et al. 2007. Mean seasonal cycle of isothermal depth in the South China Sea. *Journal of Geophysical Research: Oceans*, 112(C2): C02020, doi: [10.1029/2006JC003583](https://doi.org/10.1029/2006JC003583)
- Qu Tangdong, Girton J B, Whitehead J A. 2006. Deepwater overflow through Luzon Strait. *Journal of Geophysical Research: Oceans*, 111(C1): C01002, doi: [10.1029/2005JC003139](https://doi.org/10.1029/2005JC003139)
- Shaw P T, Chao S Y. 1994. Surface circulation in the South China Sea. *Deep-Sea Research Part I: Oceanographic Research Papers*, 41(11–12): 1663–1683
- Shu Yeqiang, Xue Huijie, Wang Dongxiao, et al. 2014. Meridional overturning circulation in the South China Sea envisioned from the high-resolution global reanalysis data GLBa0.08. *Journal of Geophysical Research: Oceans*, 119(5): 3012–3028, doi: [10.1002/2013JC009583](https://doi.org/10.1002/2013JC009583)
- Song Y T, Chao Yi. 2004. A theoretical study of topographic effects on coastal upwelling and cross-shore exchange. *Ocean Modelling*, 6(2): 151–176, doi: [10.1016/S1463-5003\(02\)00064-1](https://doi.org/10.1016/S1463-5003(02)00064-1)
- Wang J. 1986. Observation of abyssal flows in the northern South China Sea. *Acta Oceanographica Taiwanica*, 16: 36–45
- Wang Dongxiao, Liu Qinyan, Huang Ruixin, et al. 2006. Interannual variability of the South China Sea throughflow inferred from wind data and an ocean data assimilation product. *Geophysical Research Letters*, 33(14): L14605, doi: [10.1029/2006GL026316](https://doi.org/10.1029/2006GL026316)
- Xiao Jinggen, Xie Qiang, Liu Changjian, et al. 2013. A diagnostic model of the South China Sea bottom circulation in consideration of tidal mixing, eddy-induced mixing and topography. *Haiyang Xuebao* (in Chinese), 35(5): 1–13
- Xie Lingling, Pallàs-Sanz E, Zheng Quanan, et al. 2017. Diagnosis of 3D vertical circulation in the upwelling and frontal zones east of Hainan Island, China. *Journal of Physical Oceanography*, 47(4): 755–774, doi: [10.1175/JPO-D-16-0192.1](https://doi.org/10.1175/JPO-D-16-0192.1)
- Xie Qiang, Xiao Jinggen, Wang Dongxiao, et al. 2013. Analysis of deep-layer and bottom circulations in the South China Sea based on eight quasi-global ocean model outputs. *Chinese Science Bulletin*, 58(32): 4000–4011, doi: [10.1007/s11434-013-5791-5](https://doi.org/10.1007/s11434-013-5791-5)
- Xie Lingling, Zhang Shuwen, Zhao Hui. 2012. Overview of studies on Qiongdong upwelling. *Journal of Tropical Oceanography*, 31(4): 35–41
- Xu Fanghua, Oey L Y. 2014. State analysis using the Local Ensemble Transform Kalman Filter (LETKF) and the three-layer circulation structure of the Luzon Strait and the South China Sea. *Ocean Dynamics*, 64(6): 905–923, doi: [10.1007/s10236-014-0720-y](https://doi.org/10.1007/s10236-014-0720-y)
- Xu Tengfei, Wei Zexun, Susanto R D, et al. 2021. Observed water exchange between the South China Sea and Java Sea through Karimata Strait. *Journal of Geophysical Research: Oceans*, 126(2): e2020JC016608, doi: [10.1029/2020JC016608](https://doi.org/10.1029/2020JC016608)
- Yuan Dongliang. 2002. A numerical study of the South China Sea deep circulation and its relation to the Luzon Strait transport. *Acta Oceanologica Sinica*, 21(2): 187–202
- Zhang Zhiwei, Zhao Wei, Tian Jiwei, et al. 2015. Spatial structure and temporal variability of the zonal flow in the Luzon Strait. *Journal of Geophysical Research: Oceans*, 120(2): 759–776, doi: [10.1002/2014JC010308](https://doi.org/10.1002/2014JC010308)
- Zhao Wei, Zhou Chun, Tian Jiwei, et al. 2014. Deep water circulation in the Luzon Strait. *Journal of Geophysical Research: Oceans*, 119(2): 790–804, doi: [10.1002/2013JC009587](https://doi.org/10.1002/2013JC009587)
- Zhou Chun, Zhao Wei, Tian Jiwei, et al. 2014. Variability of the deep-water overflow in the Luzon Strait. *Journal of Physical Oceanography*, 44(11): 2972–2986, doi: [10.1175/JPO-D-14-0113.1](https://doi.org/10.1175/JPO-D-14-0113.1)
- Zhou Chun, Zhao Wei, Tian Jiwei, et al. 2017. Deep Western Boundary Current in the South China Sea. *Scientific Reports*, 7(1): 9303, doi: [10.1038/s41598-017-09436-2](https://doi.org/10.1038/s41598-017-09436-2)
- Zhu Yaohua, Fang Guohong, Wei Zexun, et al. 2016. Seasonal variability of the meridional overturning circulation in the South China Sea and its connection with inter-ocean transport based on SODA2.2.4. *Journal of Geophysical Research: Oceans*, 121(5): 3090–3105, doi: [10.1002/2015JC011443](https://doi.org/10.1002/2015JC011443)
- Zhu Yaohua, Sun Junchuan, Wang Yonggang, et al. 2017a. Effect of potential vorticity flux on the circulation in the South China Sea. *Journal of Geophysical Research: Oceans*, 122(8): 6454–6469, doi: [10.1002/2016JC012375](https://doi.org/10.1002/2016JC012375)
- Zhu Yaohua, Sun Junchuan, Wei Zexun, et al. 2017b. A fresh look at the deepwater overflow in the Luzon Strait. *Acta Oceanologica Sinica*, 36(5): 1–8, doi: [10.1007/s13131-017-1057-4](https://doi.org/10.1007/s13131-017-1057-4)